Mon. Not. R. Astron. Soc. **000**, 000–000 (0000) Printed 17 September 1997 (MN LATEX style file v1.4)

The mass of the white dwarf in the old nova BT Mon

D. A. Smith,[1] V. S. Dhillon,[2] T. R. Marsh[3]
[1] *Institute of Astronomy, Madingley Road, Cambridge CB3 0HA (dsmith@ast.cam.ac.uk)*
[2] *Royal Greenwich Observatory, Madingley Road, Cambridge CB3 0EZ (vsd@ast.cam.ac.uk)*
[3] *University of Southampton, Department of Physics and Astronomy, Highfield, Southampton SO17 1BJ (trm@astro.soton.ac.uk)*

Accepted for publication in the Monthly Notices of the Royal Astronomical Society, 11 September 1997

ABSTRACT
We present spectrophotometry of the eclipsing old nova BT Mon (Nova Mon 1939). By detecting weak absorption features from the secondary star, we find its radial velocity semi-amplitude to be $K_R = 205 \pm 5\,\mathrm{km\,s^{-1}}$ and its rotational velocity to be $v \sin i = 138 \pm 5\,\mathrm{km\,s^{-1}}$. We also measure the radial velocity semi-amplitude of the primary star to be $K_R = 170 \pm 10\,\mathrm{km\,s^{-1}}$. From these parameters we obtain a mass of $1.04 \pm 0.06\,\mathrm{M}_\odot$ for the white dwarf primary star and a mass of $0.87 \pm 0.06\,\mathrm{M}_\odot$ for the G8 V secondary star. The inclination of the system is found to be $82.2 \pm 3.2°$ and we estimate that the system lies at a distance of 1700 ± 300 pc. The high mass of the white dwarf and our finding that BT Mon was probably a fast nova together constitute a new piece of evidence in favour of the thermonuclear runaway model of classical nova outbursts. The emission lines are single peaked throughout the orbital cycle, showing absorption around phase 0.5, high velocity S-wave components and large phase offsets in their radial velocity curves. In each of these respects, BT Mon is similar to the SW Sex stars. We also find quasi-periodic flaring in the trailed spectra, which makes BT Mon a candidate intermediate polar.

Key words: accretion, accretion discs – binaries: eclipsing – binaries: spectroscopic – stars: individual: BT Mon – novae, cataclysmic variables.

1 INTRODUCTION

Old novae are cataclysmic binaries in which a white dwarf primary star accretes material from a red dwarf secondary star via an accretion disc or magnetic accretion stream. By definition, an old nova is an object which has been observed to have undergone a single nova outburst and then faded back to its pre-eruptive luminosity (see Warner 1995a for a review).

The thermonuclear runaway model (TNR) is the widely accepted theory of nova outbursts (see Starrfield 1989). In this model, the primary star builds up a layer of material, accreted from the secondary star, on its surface. The temperature and pressure at the base of the layer eventually become sufficiently high for nuclear reactions to begin. After ignition, the temperature rises rapidly and the reaction rates run away, to be stopped only when the radiation pressure becomes such that most of the envelope is blown away. The model predicts that the the fastest and most violent TNRs occur as a result of the high compression in the gravitational wells of the most massive white dwarfs, while slower TNRs occur on lower mass white dwarfs. As one of the primary parameters in the TNR model is the mass of the white dwarf, we are motivated to try to measure the masses of novae as a test.

The difficulties of measuring the masses of the components of cataclysmic variables are well known: they can only be measured in eclipsing systems, and to date only one old nova, DQ Her, has had its mass tightly constrained (Horne, Welsh & Wade 1993 – $M_1 = 0.60 \pm 0.07\mathrm{M}_\odot$). This was possible because the M3 V secondary star in DQ Her is easily observed through the Na I doublet around λ8190Å. DQ Her was a moderately slow nova taking 67 days to fall 2 magnitudes from its peak luminosity, so its relatively low mass ties in reasonably well with the speed of the nova, according to the TNR model.

Nova BT Mon 1939 is another bright ($V = 15.8$), eclipsing old nova and hence another obvious candidate for mass determination. It has a longer period than DQ Her so the secondary star is of an earlier spectral type, and because the accretion structures are bright, the secondary star is faint compared with the system as a whole, so we are forced to adopt different observation and analysis strategies to those of Horne et al. (1993), as described below.

2 OBSERVATIONS

On the night of 1995 January 23/24 we obtained 47 red and 49 blue spectra of the old nova BT Mon, covering ∼ 1.0

orbits from cycle 18718.87 to 18719.86 (according to our ephemeris, see section 4.1) with the 4.2-m William Herschel Telescope (WHT) on La Palma. The exposures were all around 600-s with about 15-s dead-time for the dumping of data. The ISIS spectrometer with the R1200R and R600B gratings and the TEK CCD chips gave a wavelength coverage of approximately $4570-5370$Å at 0.8Å ($50\,\mathrm{km\,s^{-1}}$) resolution in the blue arm, and $6310-6720$Å at 0.4Å ($18\,\mathrm{km\,s^{-1}}$) resolution in the red arm. We also took spectra of the spectral type templates 61 UMa (G8 V), Gleise 567 (K0.5 V), Gleise 28 (K2 V), Gleise 105 (K3 V), Gleise 69 (K5 V), EQ Vir (K5 V) and Gleise 380 (K6 V). The 1 arcsecond slit was oriented to cover a nearby field star in order to correct for slit losses. Comparison arc spectra were taken every $30-40$ min to calibrate flexure. The night was photometric and the seeing ranged from 1.5 to 3 arcseconds.

3 DATA REDUCTION

We first corrected for pixel-to-pixel variations with a tungsten lamp flat-field. After sky subtraction, the data were optimally extracted to give raw spectra of BT Mon and the comparison star. Arc spectra were then extracted from the same locations on the detector as the targets. The wavelength scale for each spectrum was interpolated from the wavelength scales of two neighbouring arc spectra. The spectra of the nearby star were used to correct for slit losses and the observations were placed on an absolute flux scale by using observations of the standard star Feige 34 (Oke 1990) taken immediately after the run.

4 RESULTS

4.1 Ephemeris

The time of mid-eclipse for our observation was determined by plotting the blue continuum light curve (see figure 2) about the eclipse (following Robinson, Nather & Kepler 1982, hereafter RNK, whose measurements were approximately in the blue), and then fitting the midpoints of chords. A linear least-squares fit to the eight eclipse timings of RNK, the timing of Seitter (1984), and our eclipse timing (all of which are presented in table 1) yield the following ephemeris:

$$\begin{array}{lll} T_{\mathrm{mid-eclipse}} = HJD\ 2\,443\,491.7159 & +\ 0.33381379\ E \\ \qquad\qquad\qquad\quad \pm\ 0.0001 & \pm\ 0.00000001 \end{array} \qquad (1)$$

We find no evidence of a non-zero value for $\dot{P}$, in agreement with Seitter (1984).

4.2 Average spectrum

The average spectrum of BT Mon is displayed in figure 1, and in table 2 we list fluxes, equivalent widths and velocity widths of the most prominent lines measured from the average spectrum.

BT Mon shows broad Balmer and He I lines and high excitation lines of He II λ4686Å and C III/N III $\lambda\lambda$4640-4650Å. The spectrum has similarities with those of other high inclination nova-likes e.g. SW Sex (Thorstensen et al. 1991) and intermediate polars e.g. FO Aqr (Marsh & Duck 1996) in that the emission lines do not show the double peaks characteristic of high-inclination accretion discs (Horne & Marsh 1986). The weak, narrow absorption features around λ6380Å and λ6620Å show no radial velocity variations and can be attributed to the interstellar medium (as BT Mon lies at a galactic latitude of -3° and at a distance of ~ 2 kpc). There is evidence for faint absorption features from the secondary star at λ5170Å and λ6500Å.

4.3 Light curves

Regions of the spectrum devoid of emission lines were selected in the red and blue ($\lambda\lambda$6390–6490Å and $\lambda\lambda$4730–4830Å). The red and blue continuum light curves for BT Mon were then computed by summing the flux in the above wavelength ranges. A third order polynomial fit to the continuum was subtracted from the red and blue spectra and the emission-line light curves were then computed by summing the residual flux between $\pm 2000\,\mathrm{km\,s^{-1}}$ for the Balmer lines, $\pm 1000\,\mathrm{km\,s^{-1}}$ for He I λ6678Å and between $\lambda\lambda$4620-4730Å for He II and C III/N III.

The resulting light curves are plotted in figure 2 as a function of phase, following our new ephemeris. The continuum shows a deep symmetrical eclipse, the blue light curve having a deeper eclipse than the red. There is no sign of an orbital hump at $\phi \sim 0.9$, as seen by Seitter (1984), but there is flickering throughout. The continuum light curves of BT Mon in the red and the blue are similar to those of the well-known eclipsing cataclysmic variables DQ Her, RW Tri and UX UMa, as noted by RNK.

The eclipses of the Balmer lines have a different shape to the continuum, there being a distinctive shoulder in the light curve as it enters eclipse. A similar shoulder is seen in the light curve of the weak He I line, but the light curve of He II shows only a hint of it. The lines are all deeply eclipsed, even appearing flat-bottomed in the Balmer and He II lines, with the eclipse in Hα being shallower than in the other lines, which almost vanish completely. There is flickering in all of the emission line light curves, and a significant drop in the Balmer and He I line flux at $\phi \sim 0.5$. The emission line light curves of BT Mon are similar to those of SW Sex (Dhillon, Marsh & Jones 1997) and the other systems in the SW Sex class, especially with regard to the phase 0.5 absorption.

4.4 Line profile evolution

We rebinned all of the spectra onto a uniform wavelength scale, and placed the data into ten binary phase bins by averaging all the spectra falling into each bin. A multiple of 2.8 was then added to each spectrum in order to displace the data in the y-direction. The result is plotted in figure 3.

The Balmer line profiles vary dramatically over one orbital cycle. The Hα line grows from a small bump at $\phi \sim 0.0$ to a narrow spike at $\phi \sim 0.2$, then evolves into a broader, multi-peaked hump at $\phi \sim 0.5$, rising again to a spike at $\phi \sim 0.7$, mirroring that at $\phi \sim 0.2$, and finally declining on the way to eclipse. Hβ and He I undergo similar changes, but they seem to be single-peaked throughout, although this could be an artifact of the lower resolution. They become narrow at $\phi \sim 0.2$ and $\phi \sim 0.7$ and broader at $\phi \sim 0.5$,

Table 1. Times of mid-eclipse for BT Mon. [1] Seitter's uncertainty is taken to be the same as ours.

Cycle (E)	HJD at mid-eclipse (2,440,000+)	O–C (secs)	Reference
0	3491.7168 ± 0.0020	81.3	RNK
3	3492.7144 ± 0.0006	−250.6	RNK
81	3518.7540 ± 0.0002	−67.0	RNK
3176	4551.9097 ± 0.0002	107.0	RNK
3179	4552.9098 ± 0.0002	−8.8	RNK
3182	4553.9125 ± 0.0002	99.9	RNK
3188	4555.9134 ± 0.0002	−71.4	RNK
3433	4637.6971 ± 0.0002	−130.1	RNK
5488	5323.6875 ± 0.0002	134.2	Seitter[1]
18719	9740.3758 ± 0.0002	−36.7	This paper

Table 2. Fluxes and widths of prominent lines in BT Mon, measured from the average spectrum.

Line	Flux $\times 10^{-14}$ erg cm^{-2} s^{-1}	EW Å	FWHM km s^{-1}	FWZI km s^{-1}
Hα	3.9 ± 0.1	28.3 ± 0.1	950 ± 100	4500 ± 500
Hβ	2.4 ± 0.1	13.1 ± 0.1	750 ± 100	3500 ± 500
He I λ6678Å	0.3 ± 0.1	2.5 ± 0.1	600 ± 100	1500 ± 500
He II λ4686Å	4.2 ± 0.1	21.4 ± 0.1	750 ± 100	4500 ± 500
C III/N III $\lambda\lambda$4640-4650Å	1.6 ± 0.1	8.5 ± 0.1	1000 ± 100	3500 ± 500

vanishing altogether at $\phi \sim 0.0$. The high excitation lines of He II and C III/N III vary little over one binary orbit, except for their total disappearance during eclipse, and seem to be single-peaked at all phases.

4.5 Trailed spectra

We subtracted the continua from the spectra using a third order polynomial fit and then rebinned the spectra onto a constant velocity interval scale centred on the rest wavelengths of the lines. The upper panels of figure 4 show the trailed spectra of the Hα, Hβ, He II λ4686Å and He I λ6678Å lines in BT Mon. Each shows the characteristic sine waves of orbital motion in the core of the emission line, but in addition to this, there are clear signs of high velocity Balmer emission moving from $\sim 2000\,\mathrm{km\,s^{-1}}$ at $\phi \sim 0$ to $\sim -2000\,\mathrm{km\,s^{-1}}$ at $\phi \sim 0.5$. The high velocity emission is also present in the He II line but is weaker. Looking at figure 4 one notices that the semi-amplitudes of the emission line cores vary, with Hα having the highest velocity semi-amplitude, Hβ the next highest, and He II the lowest. This agrees with the observations of Seitter (1984) and White, Schlegel & Honeycutt (1996). Note also the periodic flaring in the trailed spectra, visible in the horizontally striped appearance of the upper panels. This will be discussed in more detail in section 4.7. The cores of the Balmer lines almost disappear due to the phase 0.5 absorption, and the eclipse shows nothing other than the high velocity S-wave emission in the Balmer lines, which is never totally eclipsed. There are also faint components running vertically through the trailed Balmer-line spectra, which could be lines from the nebula (Marsh, Wade & Oke 1983).

4.6 Doppler tomography

Doppler tomography is an indirect imaging technique which can be used to determine the velocity-space distribution of line emission in cataclysmic variables. In this study we used the maximum entropy method to create the Doppler maps. Full technical details of the method, including a number of test simulations are given by Marsh & Horne (1988). Examples of the application of Doppler tomography to real data are given by Marsh & Horne (1990) and Marsh et al. (1990).

Figure 5 shows the Doppler maps of the Hα, Hβ, He I λ6678Å and He II λ4686Å lines in BT Mon, computed from the trailed spectra of figure 4 but with the eclipse spectra removed. The three crosses on the Doppler maps represent the centre of mass of the secondary star (upper cross), the centre of mass of the system (middle cross) and the centre of mass of the white dwarf (lower cross). The secondary star's Roche lobe and the predicted trajectory of the gas stream have been plotted using the mass ratio, $q = M_2/M_1 = 0.84$ derived in section 4.12. The series of circles along the path of the gas stream mark the distance from the white dwarf at intervals of $0.1L_1$, ranging from $1.0L_1$ at the red star to $0.1L_1$ at the point of closest approach, marked by an asterisk.

It is clear from the Doppler maps that the emission

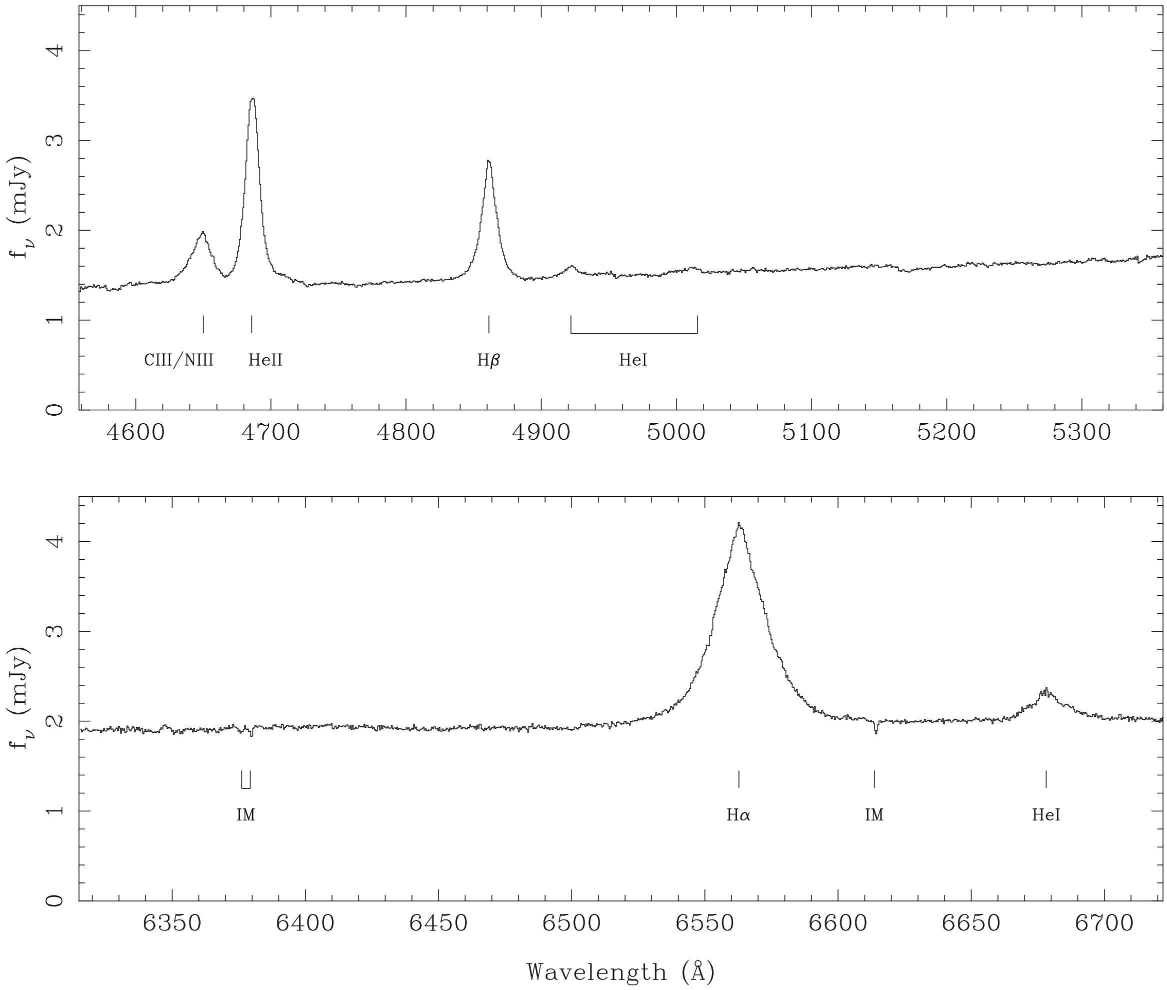

Figure 1. The average spectrum of BT Mon, uncorrected for orbital motion.

regions do not coincide with either the gas stream or the secondary star. A ring-like emission distribution, characteristic of a Keplerian accretion disc about the primary star is also absent from the maps. As in most nova-likes the bulk of the Balmer emission is mapped to the lower left quadrant of the tomogram, with the high velocity feature from the trailed spectra mapped to a zone extending out to $V_x = -2000\,\mathrm{km\,s^{-1}}$. The He II emission seems to be centred on or near the expected position of the white dwarf. A likely origin of the line emission is discussed in section 5.1.

Trailed spectra have been computed from the Doppler maps and compared to the original trailed spectra as a check. They are plotted in the lower panels of figure 4 with the eclipse spectra omitted. They compare favourably, showing the original S-waves and high velocity features.

4.7 Flares in the trailed spectra

The trailed spectra of figure 4 show periodic flaring similar to the features seen more clearly in the trailed spectra of intermediate polars e.g. FO Aqr (Marsh & Duck 1996). Because the flares are weak in BT Mon we attempted to enhance them by removing the core of the line emission and the high velocity S-wave. This was achieved by smoothing the trailed spectra images and subtracting the smoothed image from the original. The resulting trailed spectra are displayed in the top panel of figure 6 and appear to show a periodicity of ~ 30 minutes.

The flare spectra were then straightened in the velocity direction using the value of the white dwarf radial velocity found in section 4.12 ($K_W = 170\,\mathrm{km\,s^{-1}}$). The shifted spectra are plotted in the central panels of figure 6. Light curves at each wavelength were calculated for these straightened flare spectra and trailed power spectra of the three lines were then obtained by applying the Lomb-Scargle periodogram technique (Press & Rybicki 1989) to each of these light curves. The result is plotted in the bottom panels of figure 6. Hα shows no clear peaks, but the Hβ and He II λ4686Å periodograms have several peaks around 45 cycles per day, suggesting that the flares may be quasi-periodic.

The most obvious model for the multiperiodicity is that of the system being an intermediate polar, with material channelled down a magnetic accretion stream onto the magnetic pole of an asynchronously rotating primary star. The polar regions become hot, emitting X-rays which periodically light up the accretion stream/disc/curtain like a lighthouse. Further evidence, however is required to be certain of

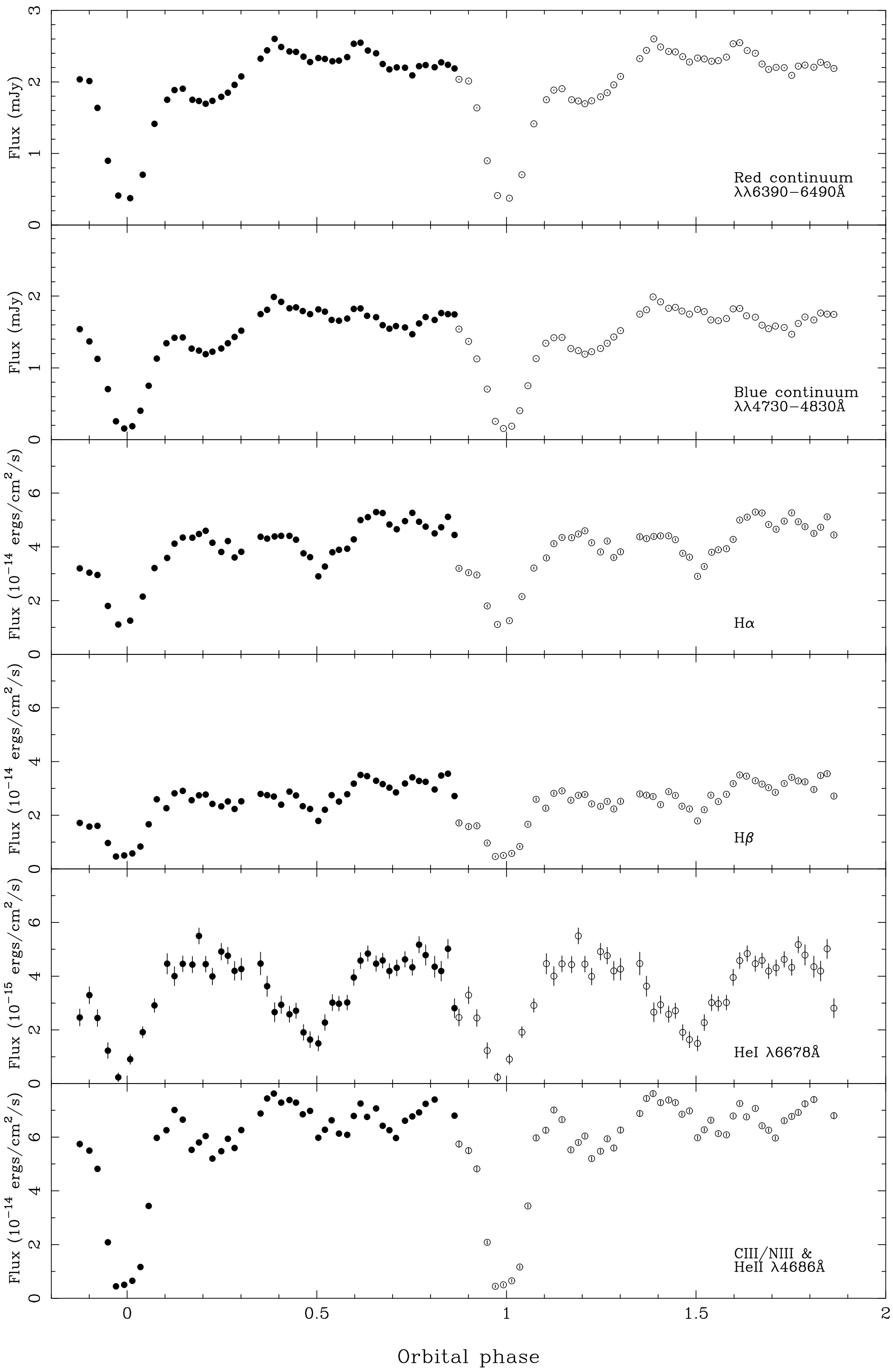

Figure 2. Continuum and emission-line light curves of BT Mon. The open circles represent points where the real data, the closed circles, have been folded over.

this classification (coherence of pulses, X-ray detection; see section 5.1).

4.8 Radial velocity of the white dwarf

The continuum-subtracted spectra were binned onto a constant velocity interval scale about each of the emission-line rest wavelengths. In order to measure the radial velocities, we used the double-Gaussian method of Schneider & Young (1980), since this technique is sensitive mainly to the motion of the line wings and should therefore reflect the motion of the white dwarf with the highest reliability. The Gaussians were of width $200\,\mathrm{km\,s^{-1}}$ (FWHM) and we varied their separation a from 400 to $3600\,\mathrm{km\,s^{-1}}$. We then fitted

$$V = \gamma - K \sin(\phi - \phi_0) \tag{2}$$

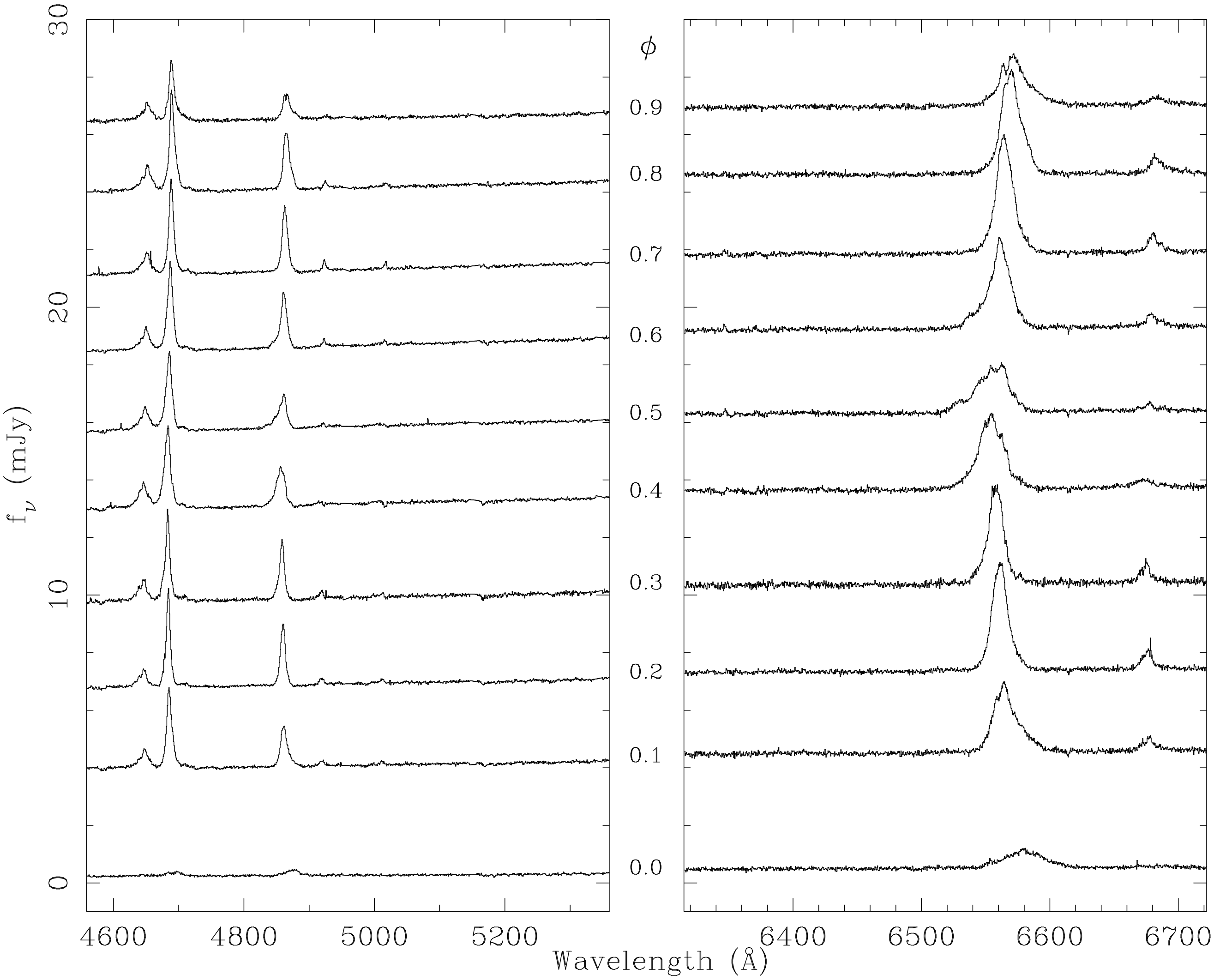

Figure 3. Orbital emission line variations in BT Mon. The data have been averaged into 10 binary phase bins with a multiple of 2.8 added to each spectrum in order to displace the data in the y-direction.

to each set of measurements, omitting 11 points near primary eclipse. Examples of the radial velocity curves obtained for Hα, Hβ, He I λ6678Å and He II λ4686Å for Gaussian separations of 1600 km s^{-1} are shown in figure 7.

The radial velocity curves of BT Mon resemble those of other novae e.g. DQ Her, and intermediate polars e.g. FO Aqr, where the superior conjunction of the emission line source, occurs after photometric mid-eclipse. This phase shift implies an emission-line source trailing the accretion disc, such as the bright-spot, and has also been observed in many nova-likes including V1315 Aql (Dhillon, Marsh & Jones 1991) and SW Sex (Dhillon et al. 1997).

The Doppler maps and light curves seem to indicate that the source of the He II λ4686Å emission is centred on the white dwarf. This would be expected, since the He II line is a high excitation feature normally only seen in high temperature regions e.g. near the surface of the white dwarf. However the radial velocity curves produced by using the double-Gaussian technique show large phase shifts. A visual inspection of the trailed spectra seems to show that it is the high velocity features in the wings which are phase shifted while the core is not. As the double-Gaussian approach to measuring the velocity would then be dominated by emission from the high velocity feature, we instead attempted to measure the radial velocity of the He II line by fitting the core of the emission line, with a single Gaussian with FWHM ranging from 50 to 800 km s^{-1}. The radial velocity curve produced using a single Gaussian of width 100 km s^{-1} is also plotted in figure 7 and shows a much lower semi-amplitude and a smaller phase shift, which appears to confirm that this emission does indeed come from close to the white dwarf.

The results of the radial velocity analysis are displayed in the form of a diagnostic diagram in figure 8. By plotting K, its associated fractional error σ_K/K, γ and ϕ_0 as functions of the Gaussian separation in the case of the double-Gaussian fits, or Gaussian FWHM in the case of the single Gaussian fits, it is supposedly possible to select the value of K which most closely matches K_W (Shafter, Szkody & Thorstensen 1986). If the emission were disc dominated, one would expect the solution for K to asymptotically reach K_W when the Gaussian separation becomes sufficiently large,

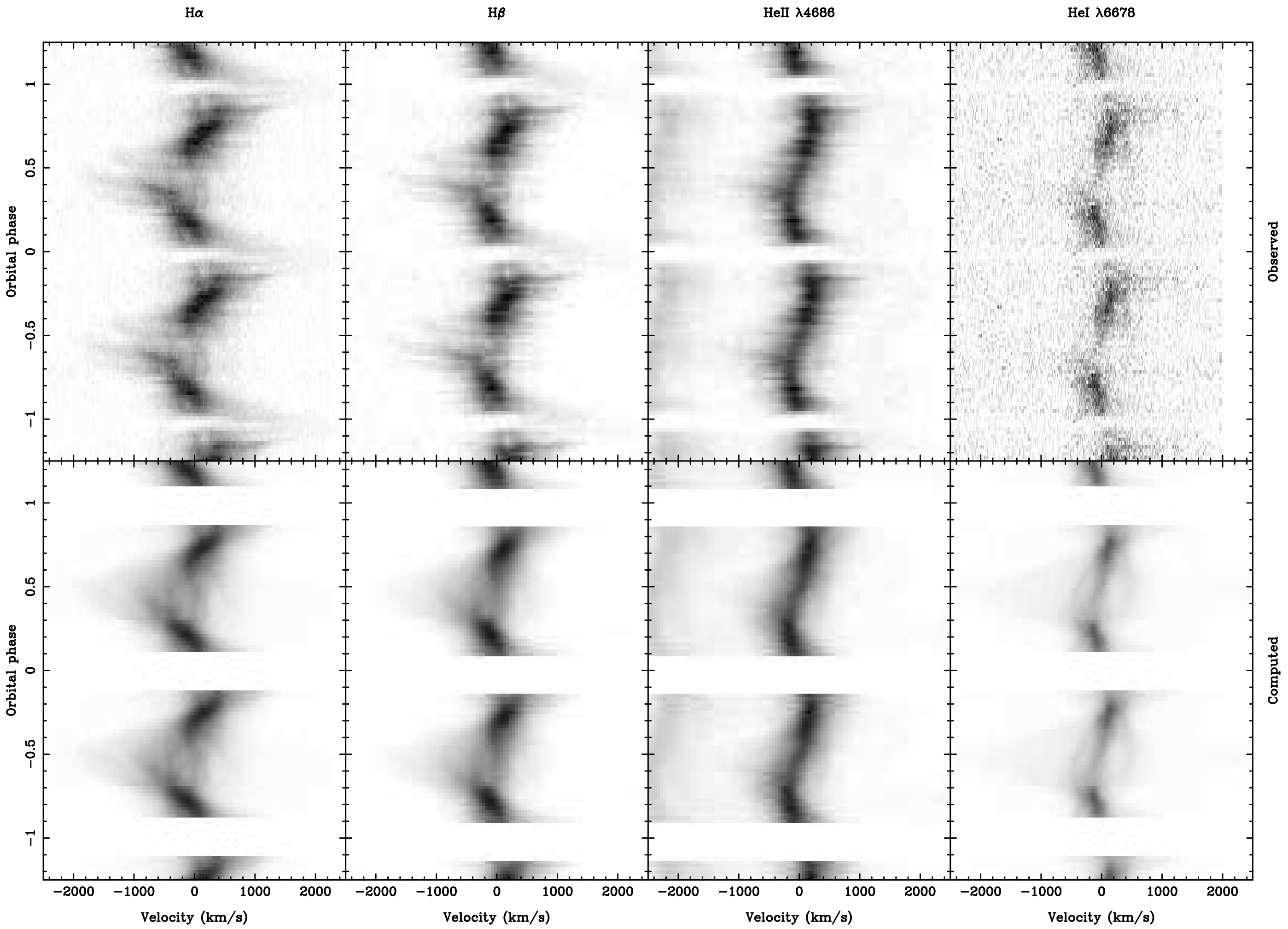

Figure 4. Trailed spectra of Hα, Hβ, He II λ4686Å and He I λ6678Å in BT Mon are displayed in the upper panels with the velocity relative to the line centre along the horizontal axis and the orbital phase along the vertical axis. The lower panels show the fits computed from the Doppler maps; the gaps correspond to eclipse data which were omitted from the fit. The data cover only one cycle, but are folded over for clarity.

and furthermore, one would expect ϕ_0 to fall to 0. This however is not the case as the phase shift ϕ_0 is over 0.1 and increases with larger double Gaussian separation. The phase shift of the single Gaussian fits for He II λ4686Å, however, do seem to fall towards zero with decreasing FWHM.

We therefore attempted to make use of a modified version of the light centres method, as described by Marsh (1988). In the co-rotating co-ordinate system, the white dwarf has velocity $(0, -K_W)$, and symmetric emission, say from a disc, would be centred at that point. By plotting $K_x = -K \sin\phi_0$ against $K_y = -K \cos\phi_0$ for the different radial velocity fits (figure 9), one finds that with decreasing values of the FWHM of the core Gaussian fit the points move closer to the K_y axis. This is because narrower Gaussian are less affected by the wings of the line and more accurately follow the radial velocity of the peak. A linear fit to the points on the light centre diagram can be extrapolated to the K_y axis to give a measurement of K_W. The extrapolation to the velocity of the white dwarf is fairly uncertain, but in figure 9 we have underplotted the Doppler tomogram. We identify the position of the peak intensity in the tomogram with the radial velocity of the white dwarf, giving a value of $K_W = 170 \pm 10\,\mathrm{km\,s^{-1}}$.

4.9 Radial velocity of the secondary star

The secondary star in BT Mon is observable through weak absorption lines, which are most clearly visible during eclipse. We compared regions of the spectra rich in absorption lines with several template red dwarfs of spectral types G8–K6, the spectra of which are plotted in figure 12. The absorption features are too weak for the normal technique of cross-correlation to be successful in finding the value of K_R, the radial velocity semi-amplitude of the secondary star, but it is possible to exploit these features to obtain an estimate of K_R using the technique of skew-mapping. This technique is described by Smith, Cameron & Tucknott (1993).

The first step was to shift the spectra of the spectral type template stars to correct for their radial velocities. We then normalised each spectrum by dividing by a spline fit to the continuum and then subtracting 1 to set the continuum to zero. The BT Mon spectra were also normalised in

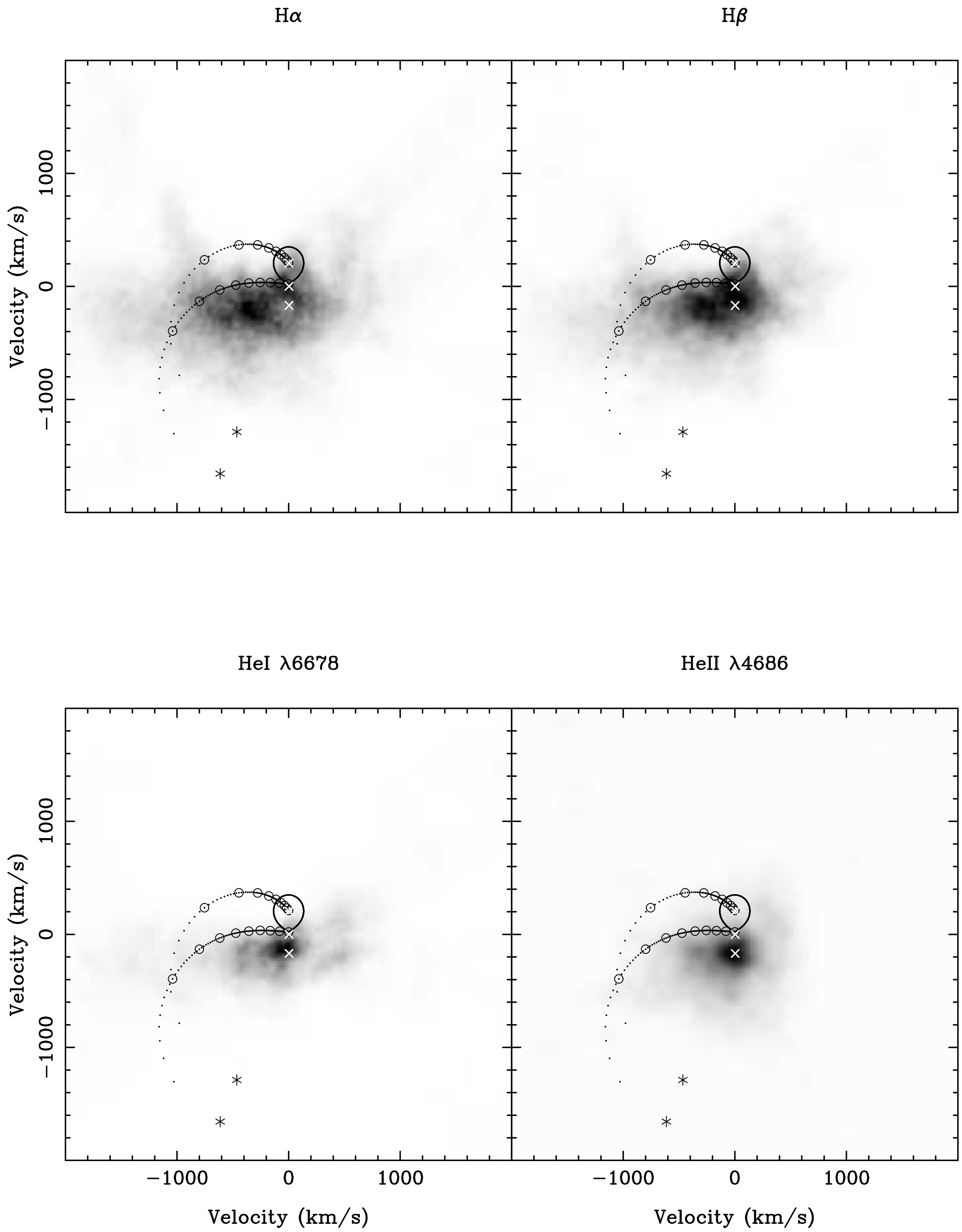

Figure 5. Doppler maps of BT Mon in Hα, Hβ, He I λ6678Å and He II λ4686Å computed from the trailed spectra in figure 4. The predicted position of the red star, the path of the gas stream (the lower curve) and the Keplerian velocity at the gas stream (upper curve) are marked. The three crosses on the map are, from top to bottom, the centre of mass of the red star, the system (at zero velocity) and the white dwarf. The emission at $\sim(-1400, -200)\,\mathrm{km\,s^{-1}}$ corresponds to the high velocity S-wave.

the same way. The template spectra were artificially broadened by $25\,\mathrm{km\,s^{-1}}$ to account for orbital smearing of the BT Mon spectra through the 600-s exposures and then by the best-fit value of the rotational velocity of the secondary star found in section 4.10, $v\sin i = 138\,\mathrm{km\,s^{-1}}$. Regions of the spectrum devoid of emission lines ($\lambda\lambda5160-5340$Å and $\lambda\lambda6400-6520$Å) were then cross-correlated with each of the templates yielding a time series of cross-correlation functions (CCFs) for each template star.

To produce the skew maps, these CCFs were back projected in the same way as time-resolved spectra in standard Doppler tomography (Marsh & Horne 1988). This is equiva-

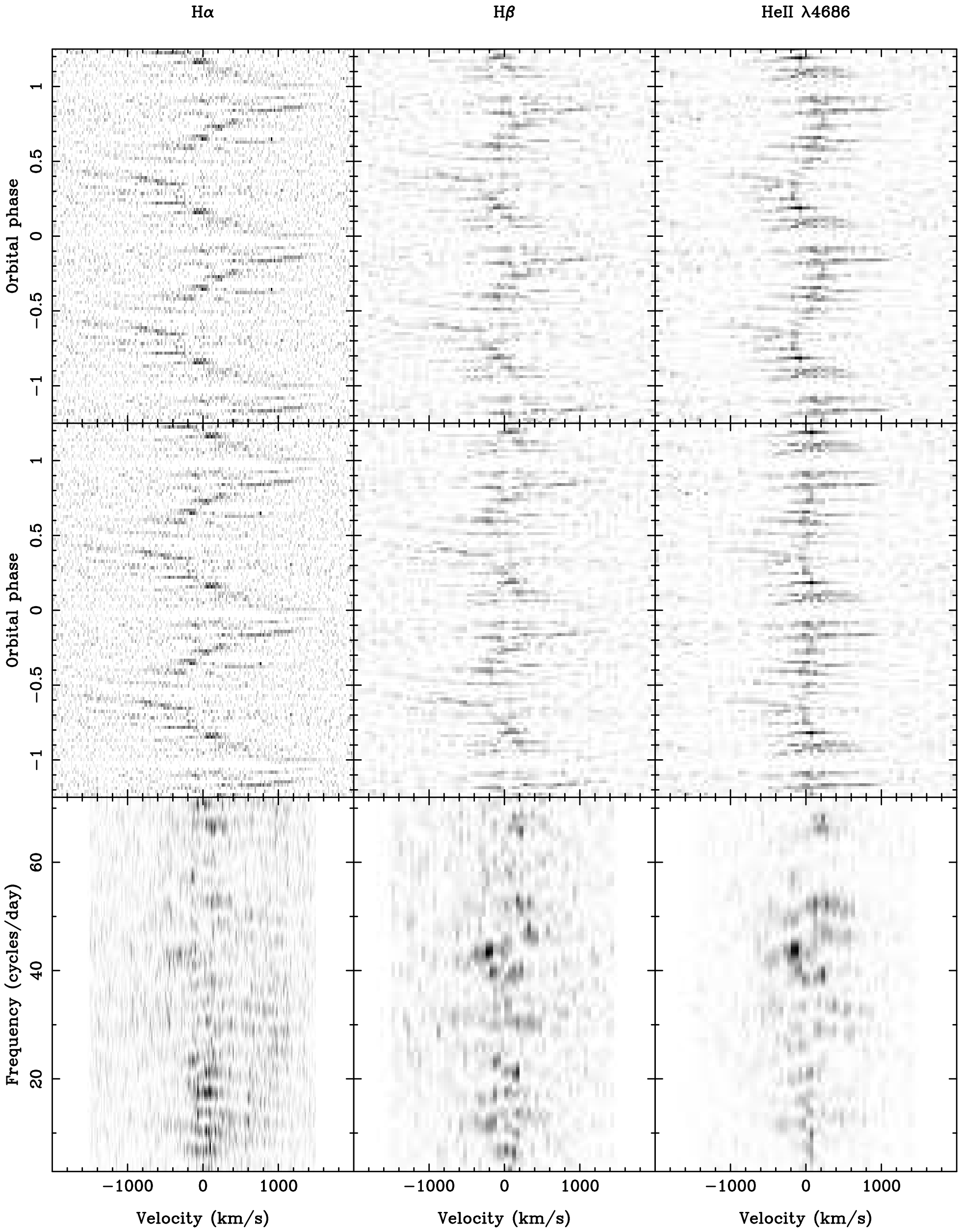

Figure 6. Upper panels: trailed spectra of Hα, Hβ, and He II λ4686Å with the flares enhanced (see text for details). Central panels: the same as the upper panels, but straightened to account for orbital motion. Lower panels: power spectra computed from the central panels at each velocity, with frequency running vertically.

lent to calculating line integrals along paths with parameter values $0 < K < 1000\,\mathrm{km\,s^{-1}}$, and $0 < \phi_0 < 1$, and then plotting the line integral values in velocity space with K as the radial co-ordinate, and ϕ_0 as the polar angle. If there is a detectable secondary star we would expect a peak at $(0,K_R)$ in the skew maps. This can be repeated for each of the templates, and the final skew-map is the one that gives the strongest peak.

When we first back-projected the CCFs, the peak in each skew map was seen to be displaced to the left by around $40\,\mathrm{km\,s^{-1}}$. The reason was that we had assumed that the centre of mass of the system was at rest. The systemic velocity of BT Mon was estimated from the diagnostic diagram to be $\gamma = 40\,\mathrm{km\,s^{-1}}$. Applying this γ velocity shifts the peak back towards the right of the skew map towards $K_x = 0$, without significantly altering K_y, i.e. the value of K_R obtained,

$$K_R = (K_x^2 + K_y^2)^{1/2} \approx K_y,\ K_x^2 \ll K_y^2$$

is almost independent of the γ assumed. This can be understood by the fact that the cross-correlation peaks are strongest at phase 0, where the eclipse spectra lie. Changing γ shifts the peak in the K_x direction but not the K_y direction. The positions of the peaks in the skew maps are plotted in figure 11 against the spectral type of the template star, for $\gamma = 0\,\mathrm{km\,s^{-1}}$, and $\gamma = 40\,\mathrm{km\,s^{-1}}$.

The skew maps produced using each of the template stars show well-defined peaks at $K_y \approx 205\,\mathrm{km\,s^{-1}}$, in both

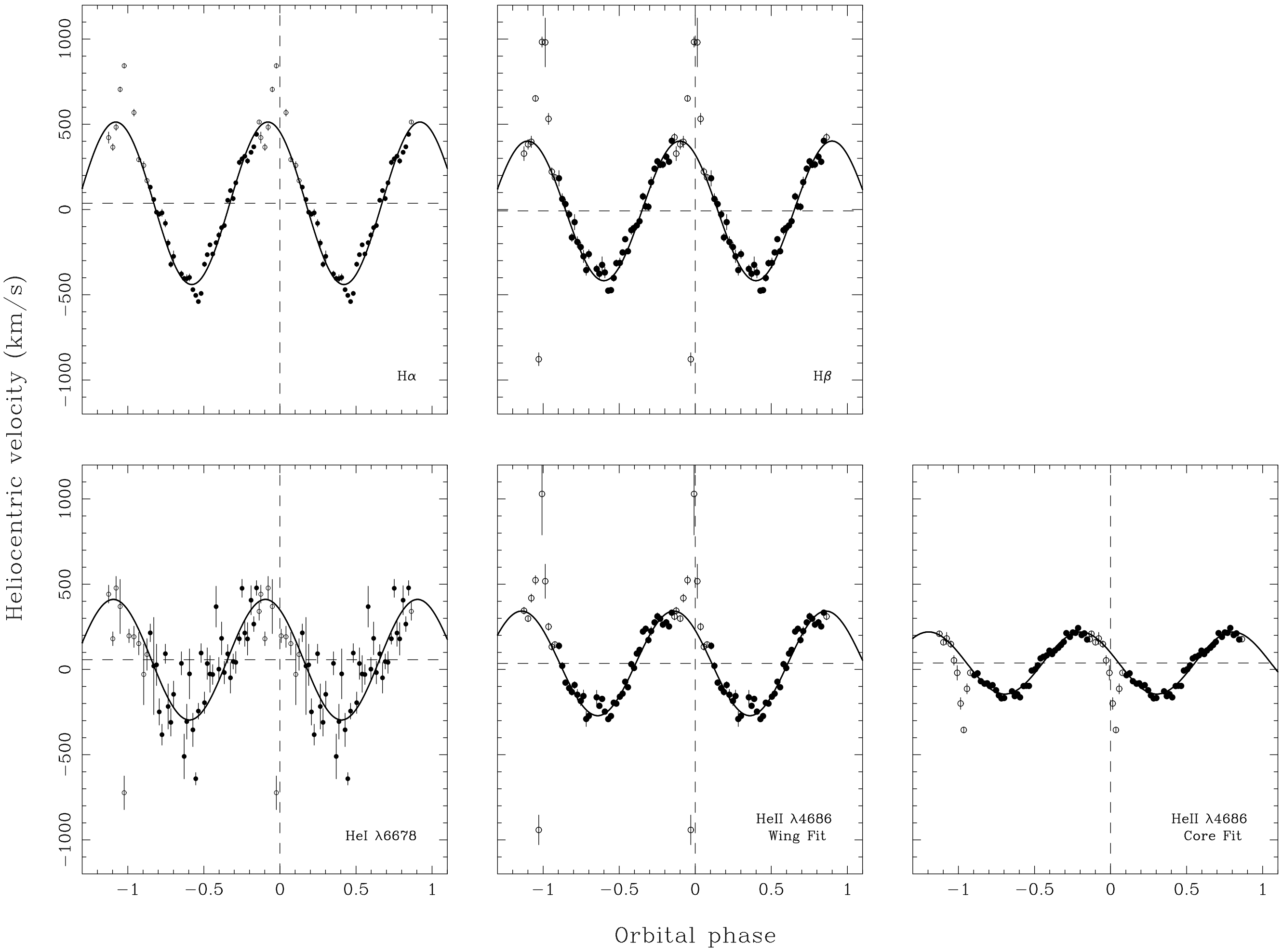

Figure 7. Radial velocity curves of Hα, Hβ, He I λ6678Å and He II λ4686Å measured using a double Gaussian fit with a Gaussian separation of 1600 $\mathrm{km\,s^{-1}}$. The bottom-right panel shows the radial velocity curve of He II λ4686Å, measured using a single Gaussian of width 100 $\mathrm{km\,s^{-1}}$ FWHM. Points marked by open circles were not included in the radial velocity fits, due to measurement uncertainties during eclipse. The horizontal dashed lines represent the systemic velocities.

the blue and red. The final skew maps for the G8 V template (found to be the best fitting template for the secondary star in section 4.10) are shown in figure 10. From the scatter of the points in figure 11, which correspond to the positions of the peaks in each skew map, we adopt a value for the radial velocity semi-amplitude of the secondary star from the skew maps of $K_R = 205 \pm 5\,\mathrm{km\,s^{-1}}$.

4.10 Rotational velocity of the secondary star

Having obtained estimates of K_W and K_R, the third measurement we made was the rotational velocity of the secondary star, $v \sin i$, which was found in the following way. Using the value of K_R obtained from the skew maps in section 4.9 we corrected for the orbital motion when averaging the four mid-eclipse spectra of BT Mon (those which show the strongest absorption features). We then broadened the template spectra to account for smearing due to the orbital motion of BT Mon over each 600-s exposure – about $25\,\mathrm{km\,s^{-1}}$ – and then rotationally broadened the templates by a range of velocities (50–200 $\mathrm{km\,s^{-1}}$). Finally we ran an optimal subtraction routine, which subtracts a constant times the normalised template spectra from the normalised, orbitally-corrected BT Mon eclipse spectrum, adjusting the constant to minimise the residual scatter between the spectra. The scatter is measured by carrying out the subtraction and then computing the χ^2 between this residual spectrum and a smoothed version of itself. By finding the value of the rotational broadening which minimises the reduced-χ^2 we obtain an estimate of both $v \sin i$ and the spectral type of the secondary star. There should, strictly speaking, be a small correction due to the intrinsic rotational velocity of the template star, but as the templates are late type stars they are assumed to be sufficiently old to have lost most of their angular momentum by magnetic braking and to have a very small $v \sin i$ (of the order of $1\,\mathrm{km\,s^{-1}}$; Gray 1992).

The value of $v \sin i$ obtained with this method depends upon several factors. Using later spectral types as templates tended to produce lower values of $v \sin i$ by up to $25\,\mathrm{km\,s^{-1}}$ in the blue band, but had a smaller effect in the red with a spread of only $6\,\mathrm{km\,s^{-1}}$. The wavelength range we used for the optimal subtraction also affected the value, as did the value of the limb-darkening coefficient used in the broaden-

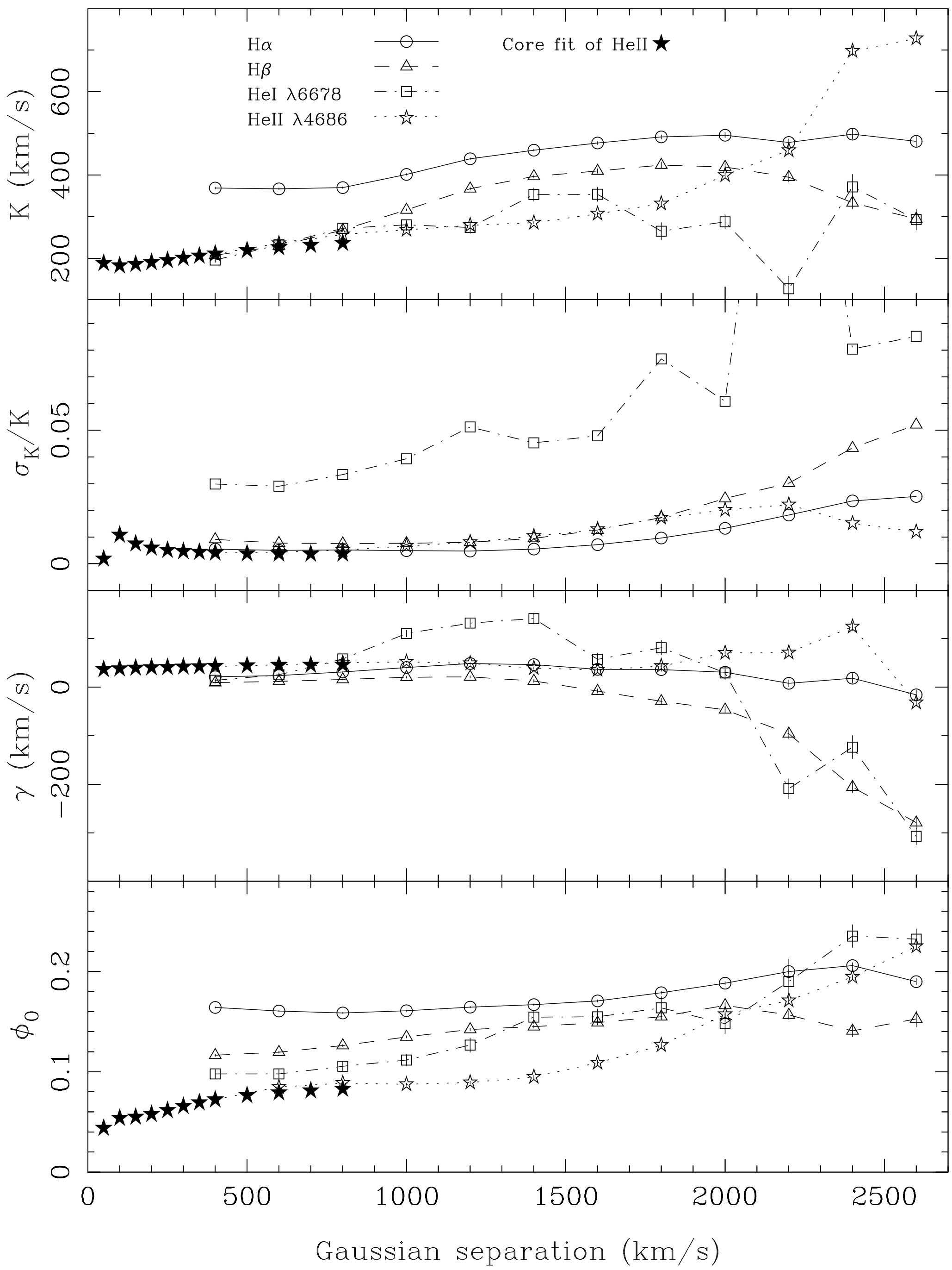

Figure 8. The diagnostic diagram for BT Mon based on the double Gaussian radial velocity fits to Hα (circles connected by solid line), Hβ (triangles connected by dashed lines), He I λ6678Å (squares connected by dashed-dotted lines) and He II λ4686Å (stars connected by dotted lines). Radial velocity fits for He II λ4686Å using a core Gaussian fit are also plotted against the FWHM in $\mathrm{km\,s^{-1}}$ with solid stars.

ing procedure, and the amount of smoothing of the residual spectrum in the calculation of χ^2 in the optimal subtraction routine. The values of $v \sin i$ for the different templates in the red and the blue wavelength ranges, calculated using values for the limb-darkening coefficient of 0.5 and the smoothing coefficient of $15\,\mathrm{km\,s^{-1}}$ are listed in table 3.

We plotted the values of χ^2 versus $v \sin i$ for each of the spectral type template stars in figure 13. The minimum of the lowest curve gives both the value of $v \sin i$ and the spectral type of the secondary star. The two wavelength ranges used give very consistent values. The blue band gives $v \sin i \approx 140\,\mathrm{km\,s^{-1}}$, and the spectral type G8 V, or possibly earlier, since we have no earlier template spectra. The red band also gives a spectral type of the secondary star of G8 V or earlier, although note the expanded vertical scale in the right hand panel, and a $v \sin i \approx 140\,\mathrm{km\,s^{-1}}$. We adopt a value of $v \sin i = 138 \pm 5$ $\mathrm{km\,s^{-1}}$ for the rotational velocity of the secondary star, with the notional errors on this

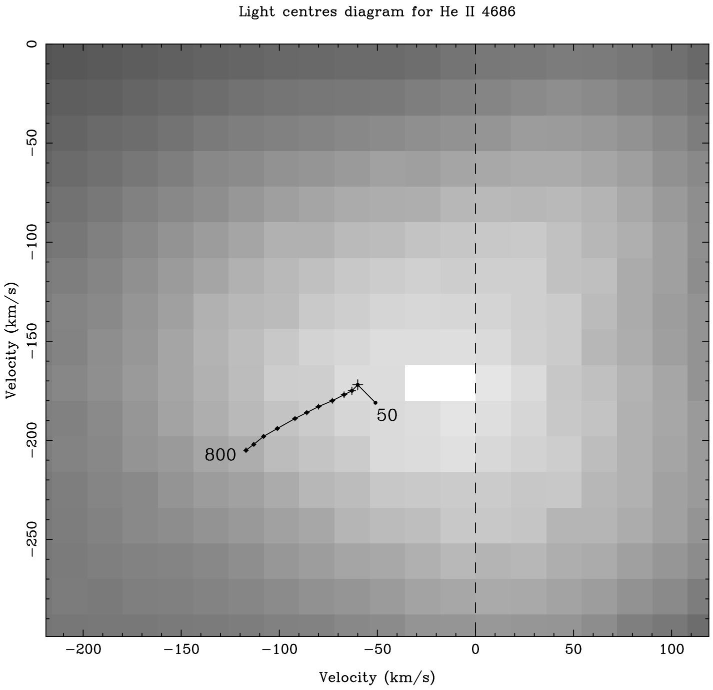

Figure 9. Light centres of the He II λ4686Å emission line in BT Mon superimposed on the Doppler tomogram. Points are plotted for radial velocity fits using single Gaussians of FWHM 50–800 km s^{-1}. The dashed line represents $K_x = 0$, and is where the white dwarf should lie.

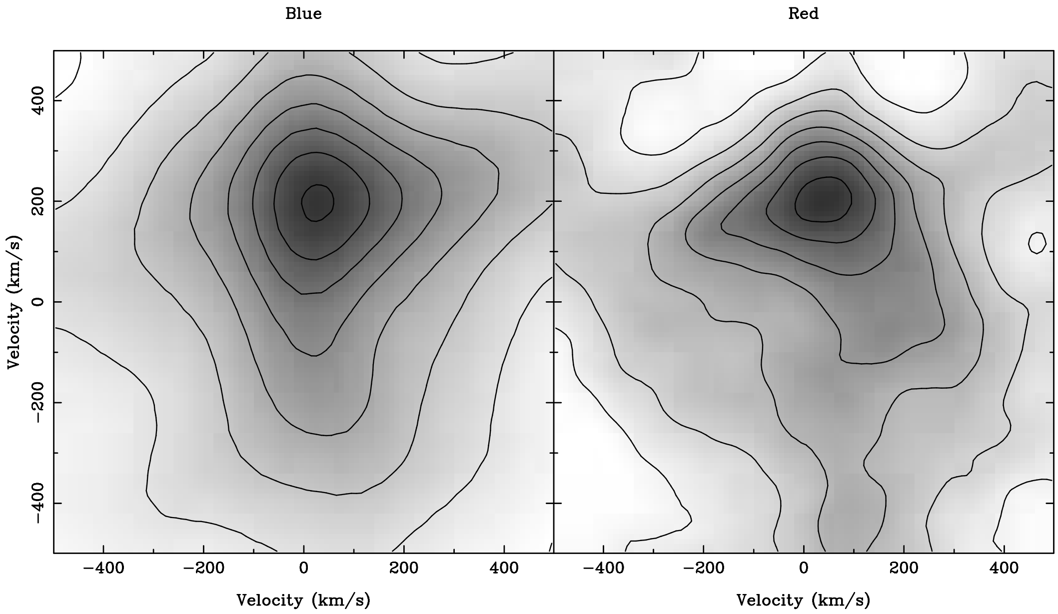

Figure 10. Skew maps of BT Mon computed by cross-correlation with the G8 V template. The cross correlations were carried out over the range $\lambda\lambda$5160–5340Å in the blue (left panel), and $\lambda\lambda$6400–6520Å in the red (right panel). A systemic velocity of 40 km s^{-1} has been assumed in each case. The value of K_R is given by the (K_x, K_y) value at the peak; $K_R^2 = K_x^2 + K_y^2$

.

estimate reflecting all of the variations noted in the previous paragraph. The spectral type of the secondary star is found to be G8 V from these $v \sin i$ curves and also from a visual comparison of the absorption line depths, the $V - R$ colour found in section 4.11, and the mass and radius found in section 4.12.

The optimal subtraction technique also tells us the value of the constant by which the template spectra were multiplied, which, for normalised spectra, is the fractional contribution of the secondary star to the total light. The results are plotted in figure 14, both in comparison with the eclipse and non-eclipse spectra. We find that the secondary star contributes 85 ± 8 per cent of the total blue light in eclipse, and 81 ± 35 per cent of the total red light in eclipse.

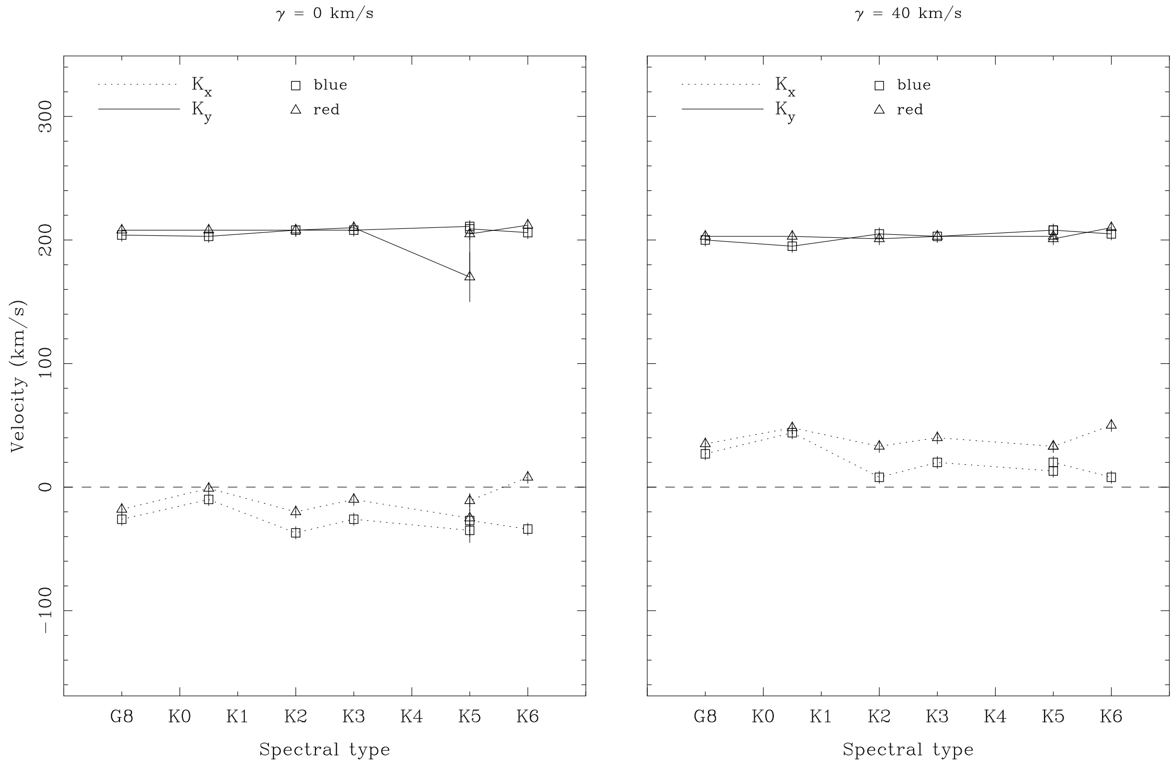

Figure 11. The position of the strongest peak in the skew maps, using $\gamma = 0\,\mathrm{km\,s^{-1}}$ (left-hand panel), and $\gamma = 40\,\mathrm{km\,s^{-1}}$ (right-hand panel) plotted against template spectral type. The skew maps produced by cross-correlation with the blue spectra (λλ5160–5340Å) are represented by squares, and those produced by cross-correlation with the red spectra (λλ6400–6520Å) are represented by triangles. The dotted lines link the K_x values and the solid lines link the K_y values.

Table 3. Values of $v \sin i$ for BT Mon as measured by comparison with the rotationally broadened profiles of G8–K6 dwarf templates. Also listed are the fractional contributions of the secondary star to the total light during eclipse, and the position of the strongest peak in the skew maps for $\gamma = 40\,\mathrm{km\,s^{-1}}$.

Template	$v \sin i$ at min χ^2 (blue) $\mathrm{km\,s^{-1}}$	$v \sin i$ at min χ^2 (red) $\mathrm{km\,s^{-1}}$	Fractional contribution of secondary (blue)	Fractional contribution of secondary (red)	(K_x,K_y) from blue skew map $\gamma = 40\,\mathrm{km\,s^{-1}}$ ($\mathrm{km\,s^{-1}}$)	(K_x,K_y) from red skew map $\gamma = 40\,\mathrm{km\,s^{-1}}$ ($\mathrm{km\,s^{-1}}$)
G8V	139	137	0.85 ± 0.08	0.81 ± 0.35	(27,200)	(35,203)
K0.5V	139	132	0.69 ± 0.07	0.53 ± 0.26	(44,195)	(48,203)
K2V	122	136	0.55 ± 0.05	0.52 ± 0.23	(8,205)	(33,201)
K3V	121	134	0.54 ± 0.05	0.52 ± 0.24	(20,203)	(40,203)
K5Ve	112	139	0.46 ± 0.05	0.38 ± 0.20	(13,208)	(33,203)
K5Vbe	121	137	0.48 ± 0.05	0.37 ± 0.19	(20,208)	(33,201)
K6V	115	133	0.47 ± 0.05	0.28 ± 0.17	(8,205)	(50,210)

4.11 The distance to BT Mon

By finding the apparent magnitude of the secondary star from its contribution to the total light during eclipse, and estimating its absolute magnitude, we can calculate the distance to BT Mon. At mid-eclipse, the apparent magnitude of the system is 17.4±0.2 in the red wavelength range, which is approximately the R band, of which the secondary star contributes 81 ± 35 per cent. In the blue (approximately the V band), the apparent magnitude is 18.0 ± 0.2 in eclipse, of which the secondary star contributes 85 ± 8 per cent. This gives us rough apparent magnitudes of $R = 17.6 \pm 0.5$ and $V = 18.2 \pm 0.3$ for the secondary star. There are a number of ways of estimating the absolute magnitude of the secondary star (Serrano 1978, Patterson 1984, Warner 1995b, Gray 1992), assuming it is on the main sequence. We took each of these into account and adopted an averaged value of the absolute magnitude of $M_V = +6.0 \pm 0.5$ for the secondary star and hence $m_V - M_V = 12.2 \pm 0.5$. Duerbeck (1981) calculated the extinction to BT Mon to be $A_V = 0.63$ magnitudes per kpc (we assume the error is small). The distance to BT Mon can then be calculated using the equation

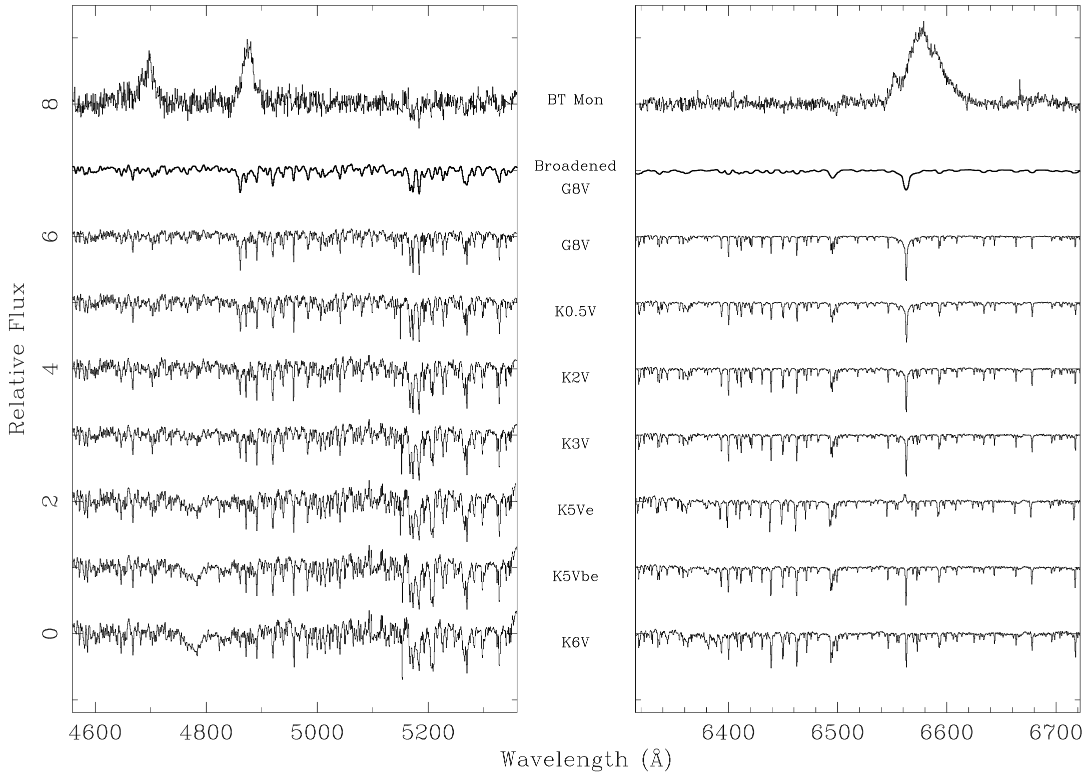

Figure 12. Normalised spectra of the seven template stars. The offset between each is 1. The uppermost spectra are a normalised average of the four mid-eclipse spectra of BT Mon, when its absorption features are most visible. The spectrum below that of BT Mon is that of the best fitting template star (G8 V) which has been broadened by 25 km s^{-1} to account for orbital smearing of the BT Mon spectra during exposure and by 138 km s^{-1} to account for the rotational broadening of the lines in BT Mon.

$$5\log(d/10) = m_V - M_V - d\,A_V/1000 \tag{3}$$

and is found to be 1700 ± 300 pc.

Another method of finding the distance is to determine the angular diameter of the secondary star from the observed flux and a surface brightness calibration that we derive from the Barnes-Evans relation (Barnes & Evans 1976).

$$F_v = 4.2207 - 0.1V_0 - 0.5\log\phi = 3.977 - 0.429(V-R)_0 \tag{4}$$

where V_0 and $(V-R)_0$ are the unreddened V magnitude and (V-R) colour of the secondary star. We take the unreddened colour to be $(V-R)_0 = 0.6 \pm 0.1$ (typical of a late G or early K dwarf) and $V_0 = 17.2 \pm 0.3$ (estimating the extinction to be 1.0 magnitudes, from above). Using these values and the radius of the secondary star derived in section 4.12 we obtain a distance of 2300 ± 700 pc.

A number of authors have estimated the distance to BT Mon. Sanford (1940) derived a value of 700–900 pc from the strengths of the interstellar H and K lines; McLaughlin (1941) assumed the radial velocities of the interstellar lines were due to the differential rotation of the Galaxy, and by also assuming that calcium was uniformly distributed along the line of sight, was able to estimate the distance to BT Mon. Using his method and the modern values for Oort's constants, RNK found a distance of 1400 pc to BT Mon. They further constrained the distance to be 1000–2000 pc by combining the value of the reddening given by Wade (1981) with the reddening versus distance curves of Deutschman, Davis & Schild (1976). Marsh, Wade & Oke (1983) estimated the distance to be ∼ 1800 pc from the expansion velocity of the nebula.

4.12 System parameters

Our measurements of the radial velocity of the secondary star, $K_R = 205 \pm 5$ km s^{-1} and the rotational broadening, $v \sin i = 138 \pm 5$ km s^{-1}, as well as our measurement of the radial velocity of the primary star $K_W = 170 \pm 10$ km s^{-1} can now be used in conjunction with our newly derived period and RNK's measurement of the eclipse full width at half depth, $\Delta\phi_{1/2} = 0.117 \pm 0.011$, to determine accurate system parameters for BT Mon. Because only four of these five measurements are needed to calculate the system parameters, and because as they stand, the measured values of these parameters are not consistent with one another, we have opted for a Monte Carlo approach similar to that of Horne et al. (1993) to calculate the masses and other parameters. For a given set of values of K_R, $v \sin i$, $\Delta\phi_{1/2}$ and P the other system parameters are calculated as follows.

Because the secondary star fills its Roche lobe, R_2/a can be estimated; R_2 is the equatorial radius of the secondary star and a is the binary separation. We used Eggleton's formula (Eggleton 1983) which gives the volume-equivalent radius of the Roche lobe to better than 1%, which is close to the equatorial radius of the secondary star as seen during eclipse;

$$\frac{R_2}{a} = \frac{0.49q^{2/3}}{0.6q^{2/3} + \ln\left(1+q^{1/3}\right)}. \tag{5}$$

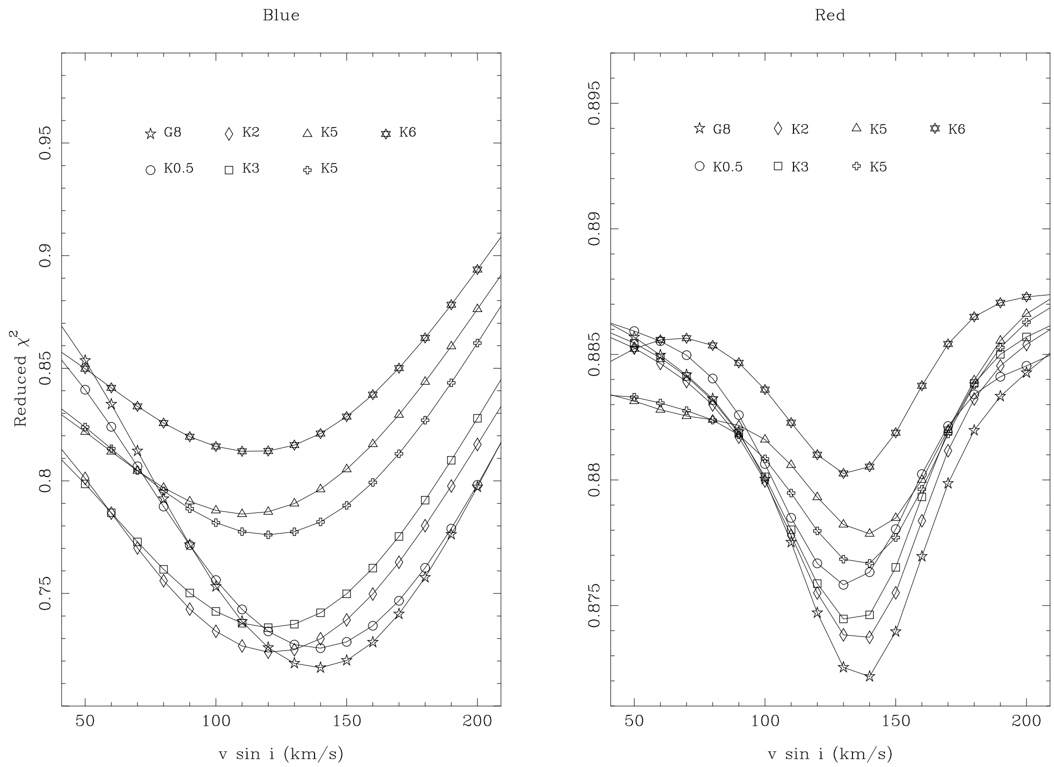

Figure 13. Reduced-χ^2 from the optimal subtraction technique plotted against $v \sin i$ for both the blue wavelength range ($\lambda\lambda$5160–5340Å, left-hand panel) and the red wavelength range ($\lambda\lambda$6400–6520Å, right-hand panel). The red band has 304 degrees of freedom, and the blue 216 degrees of freedom.

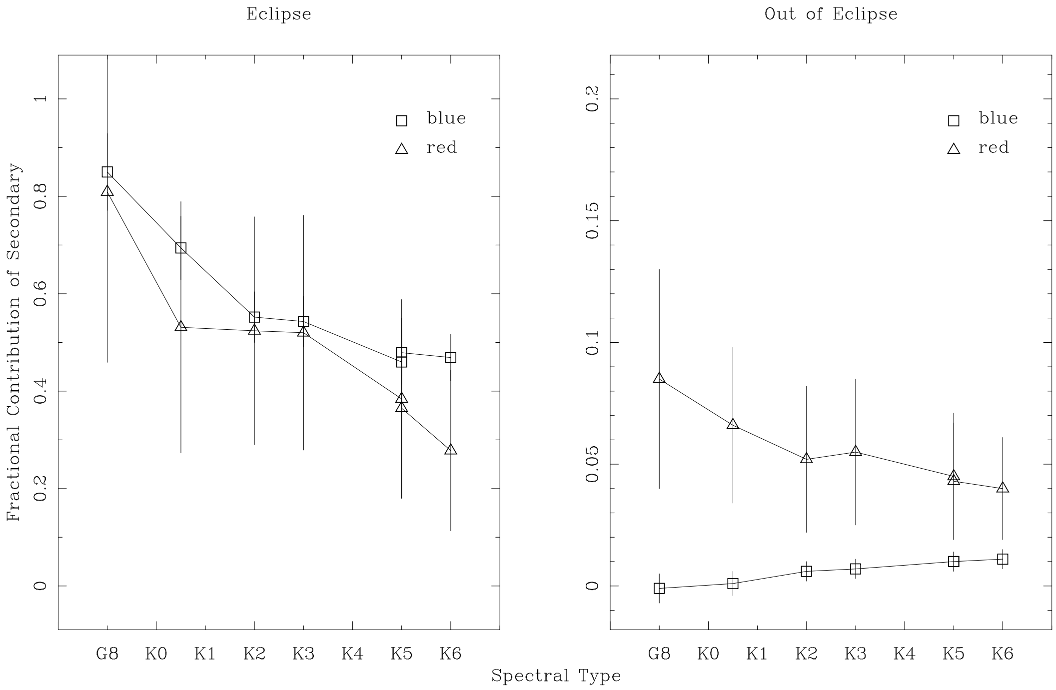

Figure 14. The fractional contribution of the secondary star to the total light in eclipse (left-hand panel) and out of eclipse (right-hand panel) in the red (plotted as triangles) and the blue (plotted as squares), as determined by the optimal subtraction of the template spectra.

The secondary star rotates synchronously with the orbital motion, so we can combine K_R and $v \sin i$, to get

$$\frac{R_2}{a}(1+q) = \frac{v \sin i}{K_R}. \tag{6}$$

This gives us two simultaneous equations so we can calculate the mass ratio q and R_2/a.

Simple geometric considerations give us

$$\left(\frac{R_2}{a}\right)^2 = \sin^2 \pi\Delta\phi_{1/2} + \cos^2 \pi\Delta\phi_{1/2} \cos^2 i. \tag{7}$$

which using the value of R_2/a obtained using equations (5) and (6) allows us to calculate the inclination of the system. Kepler's Third Law gives us

$$\frac{K_R^3 P}{2\pi G} = \frac{M_1 \sin^3 i}{(1+q)^2} \tag{8}$$

which with the values of q and i calculated using equations (5), (6) and (7), gives the mass of the primary star. The mass of the secondary star can then be obtained using

$$M_2 = qM_1. \tag{9}$$

The radius of the secondary star is obtained from the equation

$$\frac{v \sin i}{R_2} = \frac{2\pi \sin i}{P}, \tag{10}$$

and the separation of the components, a is calculated from equations (6) and (10) with q and i now known.

The Monte Carlo simulation takes 10,000 sample values of K_R, $v \sin i$ and $\Delta\phi_{1/2}$, treating each as being normally distributed about their measured values with standard deviations equal to the errors on the measurements. We then calculate the masses of the components, the inclination of the system, the radius of the secondary star, and the separation of the components, as outlined above, omitting $(K_R, v \sin i, \Delta\phi_{1/2})$ triplets which are inconsistent with $\sin i \leq 1$. Each triplet is also subject to rejection if the calculated value of K_W (implied by the triplet) is inconsistent with the measured value of K_W (implied by figure 9). This was done in accordance with a Gaussian probability law, i.e. if the calculated value of K_W lies 1σ (with σ equal to the measured error on K_W) from the mean (the measured value of K_W), the probability of rejection is 68 per cent, at 2σ it is 95 per cent, etc. Each accepted (M_1, M_2) pair is then plotted as a point in figure 15, and the masses and their errors are computed from the mean and standard deviation of the distribution of spots. The solid curves in figure 15 satisfy the white dwarf radial velocity constraint, $K_W = 170 \pm 10\,\mathrm{km\,s^{-1}}$, the secondary star radial velocity constraint $K_R = 205 \pm 5\,\mathrm{km\,s^{-1}}$ and the rotational velocity of the secondary star, $v \sin i = 138 \pm 5\,\mathrm{km\,s^{-1}}$. We find that $M_1 = 1.04 \pm 0.06\mathrm{M}_\odot$ and $M_2 = 0.87 \pm 0.06\mathrm{M}_\odot$ The values of all the system parameters deduced from the Monte-Carlo computation are listed in table 4.

The mass and radius of the secondary star are consistent within the error bars with those of a main sequence star according to the values published by Gray (1992) for a G8 dwarf ($M = 0.89\mathrm{M}_\odot$, $R = 0.88\mathrm{R}_\odot$) and the empirical relation obtained by (Warner 1995b) between mass and radius for detached stars in binaries and the secondary stars in CVs,

$$R/R_\odot = (M/M_\odot)^{13/15}. \tag{11}$$

Table 4. System Parameters for BT Mon

Parameter	**Measured Values**	**Monte Carlo Values**
P_{orb} (d)	**0.33381379**	
K_R ($\mathrm{km\,s^{-1}}$)	**205 ± 5**	**205 ± 5**
$v \sin i$ ($\mathrm{km\,s^{-1}}$)	**138 ± 5**	**136 ± 4**
$\Delta\phi_{1/2}$	**0.117 ± 0.011**	**0.109 ± 0.007**
K_W ($\mathrm{km\,s^{-1}}$)	**170 ± 10**	**171 ± 8**
q		**0.84 ± 0.04**
i°		**82.2 ± 3.2**
$M_1/M_\odot$		**1.04 ± 0.06**
$M_2/M_\odot$		**0.87 ± 0.06**
$R_2/R_\odot$		**0.89 ± 0.02**
$a/R_\odot$		**2.46 ± 0.05**
Distance (pc)	**1700 ± 300**	
Spectral type of secondary	**G8 V**	

The secondary star in BT Mon appears to be a main sequence star in all respects.

5 DISCUSSION

5.1 The nature of the system

The emission lines in the spectrum of BT Mon show single-peaked profiles, instead of the double-peaked profiles expected of high-inclination accretion discs (Horne & Marsh 1986). These profiles, and the phase 0.5 absorption in the Balmer lines are characteristics of the SW Sex stars, a class of the nova-like variables (Thorstensen et al. 1991).

There are several competing models to explain the line emission from the SW Sex objects. Honeycutt, Schlegel & Kaitchuck (1986) invoked the existence of an accretion disc wind which dominates the Balmer emission and remains unobscured during primary eclipse. Williams (1989) has suggested that the accretion disc is disrupted by a strong magnetic field due to the white dwarf, and accretion occurs via the field lines directly onto the white dwarf. The single-peaked Balmer lines would then be produced by gas flowing in an accretion curtain lying above the orbital plane. Dhillon et al. (1997) attribute the emission to an extended bright spot, the secondary star and an accretion disc. Hellier & Robinson (1994) suggests that the emission-line peculiarities of PX And and other SW Sex stars can be explained by an accretion stream which overflows the initial impact with the accretion disc and continues to a later re-impact close to the white dwarf.

The flares we have discovered in the line emission lead us to favour the intermediate polar interpretation of the system, in which material is accreted onto the magnetic poles of the primary star, giving rise to hot spots on its surface. As the white dwarf rotates asynchronously, these hot spots illuminate the inner parts of the disc, the accretion stream or the accretion curtain like a lighthouse, and we observe a flare. This is consistent with the apparent slant to the flares; if the flares were due to blobby accretion or some other form

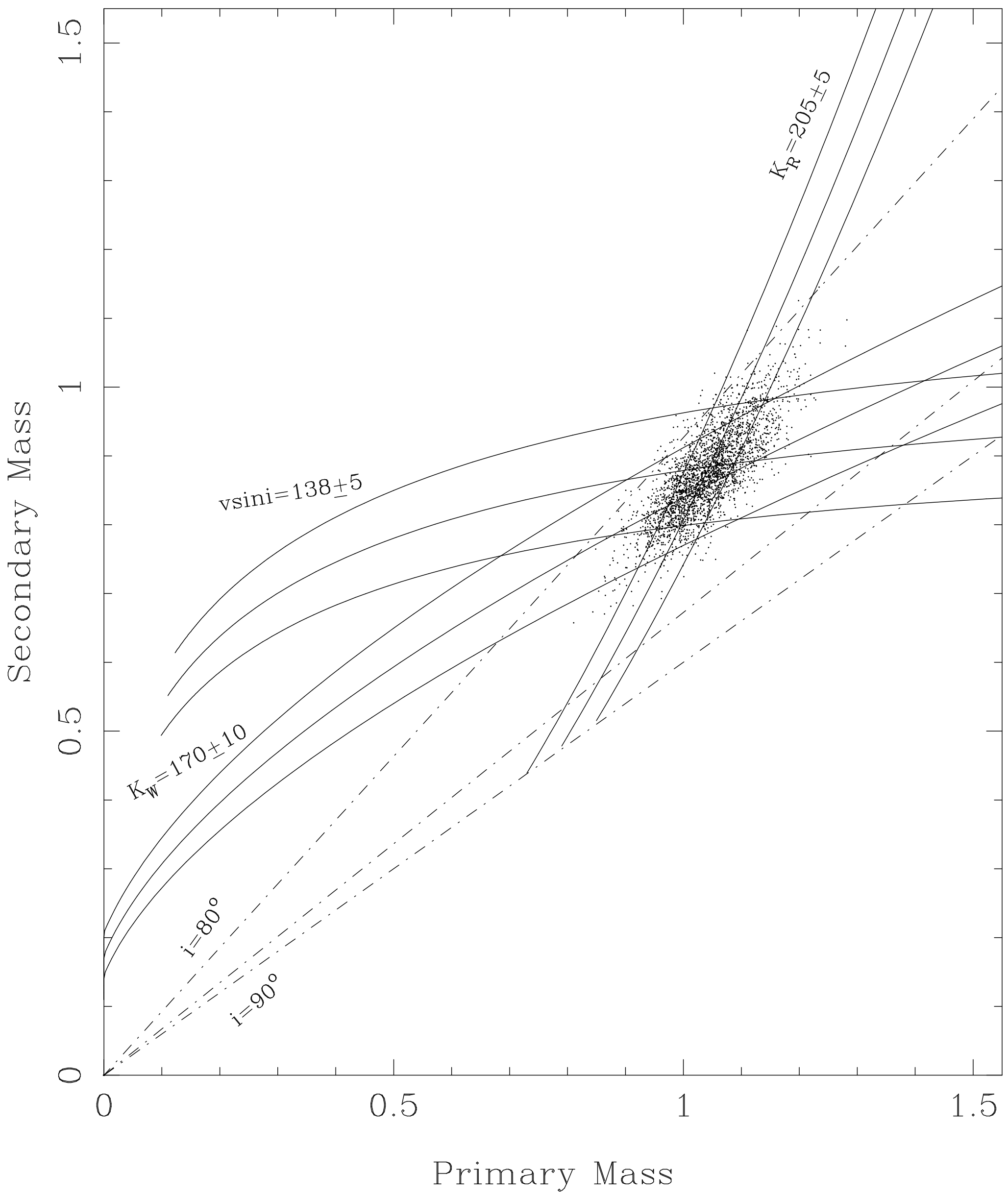

Figure 15. Constraints on the masses of the stars in BT Mon. Each dot represents an (M_1, M_2) pair. Dashed-dotted lines are lines of constant inclination (i=80°, i=85°, i=90°). The solid curves satisfy the constraints from the secondary star radial velocity $K_R = 205 \pm 5\,\mathrm{km\,s^{-1}}$, the primary star radial velocity $K_W = 170 \pm 10\,\mathrm{km\,s^{-1}}$ and the rotational velocity of the secondary star $v \sin i = 138 \pm 5\,\mathrm{km\,s^{-1}}$.

of quasi-periodic flickering then the flares would presumably appear horizontal in the trailed spectra. White et al. (1996) dismissed the IP model for BT Mon, which identifies the high velocity emission as coming from a magnetic accretion funnel, because the high velocity spike they observed in the radial velocity curve suggested to them that the feature only appeared during eclipse, whereas in our data it is visible, as it should be according to this model, throughout the whole orbital cycle. It would be of interest to search for the flares seen in BT Mon in the SW Sex stars.

The high velocity component we see in the Balmer emission of BT Mon is visible throughout the orbital cycle and does not appear to be eclipsed, implying that the source lies above the orbital plane. It is similar to that seen in some polar systems e.g. HU Aqr (Schwope, Mantel & Horne 1997), in which the source of the high velocity emission is thought to be the magnetic accretion funnel. An accretion funnel may be the source of the high velocity component in BT Mon, or it may come from the accretion stream overflowing the (undetected) disc, as suggested by Hellier & Robinson (1994) as a possible mechanism for the SW Sex stars, but our Doppler maps are not fully consistent with BT Mon satisfying either of these models.

For us to be sure of the classification of BT Mon as an intermediate polar, the flares need to be observed to be coherent, and our data set has neither the time resolution nor the baseline to give positive evidence of coherence. The system would also be expected to show X-ray pulsations and if it were strongly magnetic, circular and linear polarisation (not observed by Stockman et al. 1992). The luminosity of

BT Mon in soft X-rays is low since it has not been detected by *ROSAT* in a survey of classical novae (Marina Orio, private communication). BT Mon lies at a low galactic latitude at a distance of ~ 2 kpc, so even if it were intrinsically luminous in X-rays, it is possible that the high level of extinction would severely diminish its apparent brightness in the soft X-ray band although hard X-rays should still be visible.

5.2 The TNR model

The motivation for studying BT Mon was to obtain a tight constraint on the mass of the white dwarf, which we have done successfully, in order to test the thermonuclear runaway model for novae outbursts, which broadly predicts that the higher the mass of the white dwarf, the faster the nova outburst. Unfortunately the literature is divided over the speed class of BT Mon.

Nova Mon 1939 was not discovered until 1939 Oct 8 (Sanford 1940), by which time it had declined from its maximum brightness to around 8th or 9th magnitude, its rise to maximum failing to be observed because this occurred when it was in the daytime sky. Schaefer & Patterson (1983) looked back over archival photographic plates, taken in the month prior to the first observations by Whipple (1940), which they believed to show the nova at maximum light, with a magnitude of 8.5 (although Duerbeck 1987a notes an observation which gives the magnitude of BT Mon as 7.6), and combined these with later observations to produce an eruption light curve which suggests BT Mon was a slow nova, giving t_2 = 140 days, and t_3 = 190 days, where t_2 and t_3 are the times for the nova to decline by 2 and 3 magnitudes from its maximum brightness.

This contradicts the earlier work of McLaughlin (1941) who compared the spectra of 1939 Dec 26 and 1940 Jan 17 to those of other novae. Assuming normal behaviour, the spectra of BT Mon corresponded to declines of 5.4 magnitudes and 5.9 magnitudes, respectively, from maximum. The observed apparent magnitudes were 9.6 and 10.0 (Whipple 1940) which tells us that the faintest it could have been at maximum brightness was an apparent magnitude of 4.2. McLaughlin extrapolated the light curve back, and found that it corresponded to that of a fast nova; he later published a value for t_3 of 36 days (McLaughlin 1945).

One possible resolution of this problem is to image the nebula. Fast novae generally give rise to almost spherical shells, slow novae to more aspherical shells (Slavin, O'Brien & Dunlop 1995; Lloyd, O'Brien & Bode 1997). An image of the shell of BT Mon has been obtained by Duerbeck (1987b), who found it to be very weak with a nearly circular outline, which makes us favour the interpretation of BT Mon as a fast nova.

6 CONCLUSIONS

We have shown that BT Mon has a white dwarf with a high mass ($1.04 \pm 0.06 M_{\odot}$) and that the observational evidence supports the classification of BT Mon as a fast nova, in keeping with the thermonuclear runaway model of nova outbursts. The calculated mass and radius, and the spectral features of the secondary star, are all consistent with it being a G8 main sequence star. We have also found weak, regular flaring in the line emission, which could indicate that the system is an intermediate polar.

ACKNOWLEDGEMENTS

We are indebted to Marina Orio for the communication of the results of her BT Mon ROSAT observations. DAS is supported by a PPARC studentship and TRM by a PPARC advanced fellowship. The WHT is operated on the island of La Palma by the Royal Greenwich Observatory in the Spanish Observatorio del Roque de los Muchachos of the IAC.

REFERENCES

Barnes T., Evans D. S., 1976, MNRAS, 174, 489
Deutschman W. A., Davis R. J., Schild R. E., 1976, ApJS, 30, 97
Dhillon V. S., Marsh T. R., Jones D. H. P., 1991, MNRAS, 252, 342
Dhillon V. S., Marsh T. R., Jones D. H. P., 1997, MNRAS, in press
Duerbeck H., 1981, PASP, 93, 165
Duerbeck H., 1987a, Space Sci. Rev., 45, 1
Duerbeck H., 1987b, ESO Messenger, 50, 9
Eggleton P., 1983, ApJ, 268, 368
Gray D. F., 1992, The Observation and Analysis of Stellar Photospheres. Cambridge University Press, Cambridge
Hellier C., Robinson E. L., 1994, Astrophys. Lett., 431, 107
Honeycutt R. K., Schlegel E. M., Kaitchuck R. H., 1986, ApJ, 302, 388
Horne K., Marsh T. R., 1986, MNRAS, 218, 761
Horne K., Welsh W. F., Wade R. A., 1993, ApJ, 410, 357
Lloyd H. M., O'Brien T. J., Bode M. F., 1997, MNRAS, 284, 137
Marsh T. R., Duck S. R., 1996, New Astron., 1, 97
Marsh T. R., Horne K., 1988, MNRAS, 235, 269
Marsh T. R., Horne K., 1990, ApJ, 349, 593
Marsh T. R., Horne K., Schlegel E. M., Honeycutt R. K., Kaitchuck R. H., 1990, ApJ, 364, 637
Marsh T. R., Wade R. A., Oke J. B., 1983, MNRAS Lett., 205, 33
Marsh T. R., 1988, MNRAS, 231, 1117
McLaughlin D. B., 1941, ApJ, 93, 417
McLaughlin D. B., 1945, PASP, 57, 69
Oke J. B., 1990, AJ, 99, 1621
Patterson J., 1984, ApJS, 54, 443
Press W. H., Rybicki G. B., 1989, ApJ, 338, 277
Robinson E. L., Nather R. E., Kepler S. O., 1982, ApJ, 254, 646
Sanford R. F., 1940, PASP, 52, 35
Schaefer B. E., Patterson J., 1983, ApJ, 268, 710
Schneider D. P., Young P., 1980, ApJ, 238, 946
Schwope A. D., Mantel K.-H., Horne K., 1997, A&A, 319, 894
Seitter W. C., 1984, Ap&SS, 99, 95
Serrano A., 1978, Ph.D. thesis. University of Sussex
Shafter A. W., Szkody P., Thorstensen J. R., 1986, ApJ, 308, 765
Slavin A. J., O'Brien T. J., Dunlop J. S., 1995, MNRAS, 276, 353
Smith R. C., Cameron A. C., Tucknott D. S., 1993, in Regev O., Shaviv G., eds, Cataclysmic Variables and Related Physics. Inst. Phys. Publ., Bristol, p. 70
Starrfield S. in Bode M. F., Evans A., eds, Classical Novae, p. 39, John Wiley & Sons Ltd., Chichester, 1989
Stockman H. S., Schmidt G. D., Berriman G., Liebert J., Moore R. L., Wickramasinghe D. T., 1992, ApJ, 401, 628

Thorstensen J. R., Ringwald F. A., Wade R. A., Schmidt G. D., Norsworthy J. E., 1991, AJ, 102, 272
Wade R. A., 1981, Ph.D. thesis. California Institute of Technology
Warner B., 1995a, Cataclysmic Variable Stars. Cambridge University Press, Cambridge
Warner B., 1995b, Ap&SS, 232, 89
Whipple F., 1940, Harvard Bull., 912, 5
White J. C., Schlegel E. M., Honeycutt R. K., 1996, ApJ, 456, 777
Williams R. E., 1989, AJ, 97, 1752